

Numerical and Experimental Study of Flow Structure and Cooling Behavior of Air Impingement on a Target Plate

Adnan A. Abdul Rasool^a, Jirunthanin V.^b, F. A. Hamad^b

^aMech. Eng. Dept, college of Engineering, Al-Mustansiriya University, Baghdad, Iraq

^bSchool of Science & Engineering, Teesside University, Middlesbrough, TS1 3BA, UK

Abstract

Numerical and experimental study is carried out to investigate flow structure and heat transfer of air jet normally impinging on a flat plate. Three orifices of 5, 10 and 20 mm diameters and Z/d ratios in the range of 2 to 8 were used. The numerical simulations were performed with the ANSYS FLUENT for steady, three-dimensional, incompressible, and turbulent flow from the jet. The comparison of CFD predictions with experimental results show that a good agreement of the average Nusselt number, the pressure coefficients distributions, radial velocity distributions of the jet.

Keywords: CFD simulation, Nusselt number, jet flow, Wall jet velocity

1. Introduction

Air impingement is one of the efficient solutions of cooling hot objects in industrial processes as it produces higher heat transfer rate through forced convection. Jet impingement was used in cooling of turbine blades, quenching of steel and glass products in production line and the enhancement of cooling efficiency in the electronic industry. Heat transfer by impingement is also studied as side effects of vertical/ short take-off and landing of aircraft.

The flow structure and the mechanism of heat transfer have been studied experimentally by a number of researchers. San et al [1] carried out an experimental study of air impingement on a flat plate that flow through two exits in opposite directions. Four orifices of 3, 4, 6 and 9 mm diameters were used with jet Reynolds number in the range of 30000 – 67000 at orifice-to-plate distance /diameter, $Z/d = 2$. The results showed that for the same Reynolds number, the smaller orifice diameter give lower Nusselt number but the influence decreased for $d > 6$ mm. The measured local surface temperature shows that transition from impingement region to a wall jet region take place at (r/d) values close to 1.0. Goldstien and Bahbahani [2] reported local heat transfer coefficients measured on a plate exposed to an impinging air jet from orifice diameter, $d=12$ mm with and

without a cross flow. The results show that the peak heat transfer coefficient disappeared with cross flow at the large Z values but it increased at small Z values with cross flow. Lee et al [3] examine the heat transfer from a flat plate to a fully developed axisymmetric impinging jet from a nozzle of 11 mm diameter at different Z/d ratios. The correlation of Nusselt number with Re^n at stagnation point shows that n has values in the range of 0.5-0.7 depending on Z/d ratio. The secondary peak of heat transfer rate was observed at the hydrodynamic transition region of flow from laminar to turbulent conditions. It was observed for $Z/d < 3$ and its location shifted towards the stagnation point when Z/d decreased. Lytle & Webb [4] measured local heat transfer coefficients and static pressure distribution for nozzle diameters of 6.9 and 10.9 mm at low Z/d ratios. It was noticed that pressure decreased with radial distance from stagnation point and reached negative values at the outward positions for high jet velocities. They found that the variation of Nusselt number on the target plate were varied with the type of flow encountered at impinging point and the location of flow transition point and turbulence levels in the flow.

Anwarullah et al [5] investigated the effect of nozzle-to-surface spacing of the electronic components and Reynolds number on the heat transfer in cooling of electronic components by an impinging submerged air jet experimentally. Reynolds number based on a nozzle of 5 mm diameter is varied in the range of

* Corresponding author. Tel.: +44 1642342495

+44 1642 342401; E-mail: f.hamad@tees.ac.uk

© 2014 International Association for Sharing Knowledge and Sustainability

DOI: 10.5383/ijtee.08.01.005

6000 to 23000 while the distance from the nozzle-to-surface varied from 2 to 10 nozzle diameters. The results showed that heat transfer rate increases as the jet spacing decreases owing to the reduction in the impingement surface area.

Numerical investigation of the turbulent jet impingement on flat surfaces and associated heat transfer using various turbulence models becomes preferable due to developments in computer technology. However, the results depend significantly on the turbulence model, near-wall treatment, numerical method, and other assumptions in numerical models [6]. Behina et al [6, 7] studied the flow and heat transfer in circular confined and unconfined impinging jet configurations. Their results showed that the effect of confinement is only significant at very low Z/d (< 0.25). The flow characteristics from the orifice strongly affected the heat transfer rates, especially in the stagnation region with 30 % difference in Nusselt number was obtained using different velocity profiles. Baydar and Ozmen [8] conducted an experimental and numerical study for deepen the flow of a confined jet impinging perpendicularly the upper surface of the cavity. The mean velocity, turbulence intensity and pressure distributions in the stagnation zone were determined for Reynolds numbers ranging from 30,000 to 50,000 and for the dimensionless impinging distance between 0.2 and 6. Their results show that sub atmospheric region occurs on the impingement plate at nozzle to plate spacing up to 2 for the range of Reynolds numbers studied. The numerical results using the $K-\epsilon$ turbulence model are in agreement with the experimental results except for $Z/d < 1$. Ramezanpour et al [9] compared the basic Reynolds stress model (RSM) and renormalization group (RNG $k-\epsilon$) model in FLUENT 6.0 for a slot nozzle impinging jet on flat and inclined plates. They found that predicted Nusselt numbers from the RSM model in the impinging region and some parts of the wall jet regions show better agreement with experiments, while those predicted with the RNG $k-\epsilon$ model show a sharper reduction from the maximum point. However, in the wall jet region, the RNG $k-\epsilon$ model shows a better result than the RSM model. Angioletti et al [10] studied heat transfer numerically using RNG $k-\epsilon$, Shear Stress Transport ($k-\omega$ SST) and RSM turbulence models. They found that $k-\omega$ SST turbulence model is more reliable especially at the low Re for both the flow field and the local Nu distribution. For the higher Re , the agreement with the experimental data was improved by using RNG $k-\epsilon$ or RSM turbulence models when simulating the flow field, whereas all models were largely inadequate in the heat transfer predictions. Pulat et al [11] investigated the use of different turbulence models and near-wall treatments in modelling the heat transfer of the impingement jet. The comparison of predictions with experimental data shows that $k-\epsilon$ model is the best model can be used to simulate the experimental cases.

The purpose of this paper is to study the heat transfer from a flat plate at a constant heat flux to a turbulent impinging jet. Firstly, to identify the appropriate cell size and turbulence model by benchmarking the experimental case for orifice diameter, $d = 10$ mm and $Z/d = 6$. This particular set of experimental data is used as it is close to the most widely used

experimental data of impinging jet on a flat plate at $Re = 23000$ and $Z/d = 6$ in literature [6]. The volume of the cell is determined from the grid dependence study carried out to give the best results compared to the experimental data using RNG $k-\epsilon$ model as recommended by previous researchers. Three turbulence models including standard $k-\epsilon$, RNG $k-\epsilon$ and RSM are also used to confirm that RNG $k-\epsilon$ model gives the best data results to the experimental data. Secondly, the CFD model is used to carry out parametric study to investigate the effect of orifice diameter and turbulence on heat transfer utilizing the details data produced from the model. Thirdly, to study the effect of nozzle diameter on heat transfer for the same Reynolds number.

2. Experimental Facility

The experimental facility shown in Figure 1 is used to collect the experimental data. The air is supplied by a centrifugal blower (1) through a PVC pipe (2) of 100 mm diameter and 1.5 m length to the orifice plate (3). A Pitot tube (4) of 1.0 mm inner diameter is mounted on a traversing mechanism to measure the radial velocity distribution of the jet at different axial positions from the orifice exit. A variable inclination manometer (5) is used to measure the dynamic head across both the impinging jet and the wall jet region. A second traversing mechanism is used to control the radial position of Pitot tube (6) to measure the radial velocity distribution at different distances from plate surface. The orifice to plate distance Z is varied by changing the position of the target plate relative to the orifice. The velocity distribution within the impinging jet is measured at the same axial positions used for the target plate.

The heat transfer target plate (7) made of steel of 100 x 150 x 1 mm size fitted with thermocouples (8) of type K connected to the output recorder (9) to measure the radial temperature distributions which are used to calculate the local heat transfer coefficient and Nusselt number from the plate. The back of the plate is wrapped with 0.2 mm diameter heater silk of 15 Ω/m resistance. The back face of the plate is thermally insulated using a 40 mm thick layer of polyurethane. Thermocouples are fixed at the centre of the plate and in the radial direction with a distance of 10 mm from each other. A digital multimeter (10) is used to measure the voltage and current across the resistance of the heating silk wire. The front face of the heated plate is facing the air impinging jet with a centreline alignment relative to the jet. A DC power supply (11) is used for heating the silk wire in the present work. The electrical power supplied to the heater can be calculated as

$$p = VI \quad (1)$$

The electrical power consumed by the heater is dissipated through the plate by conduction. The total heat transfer from the plate can be written as

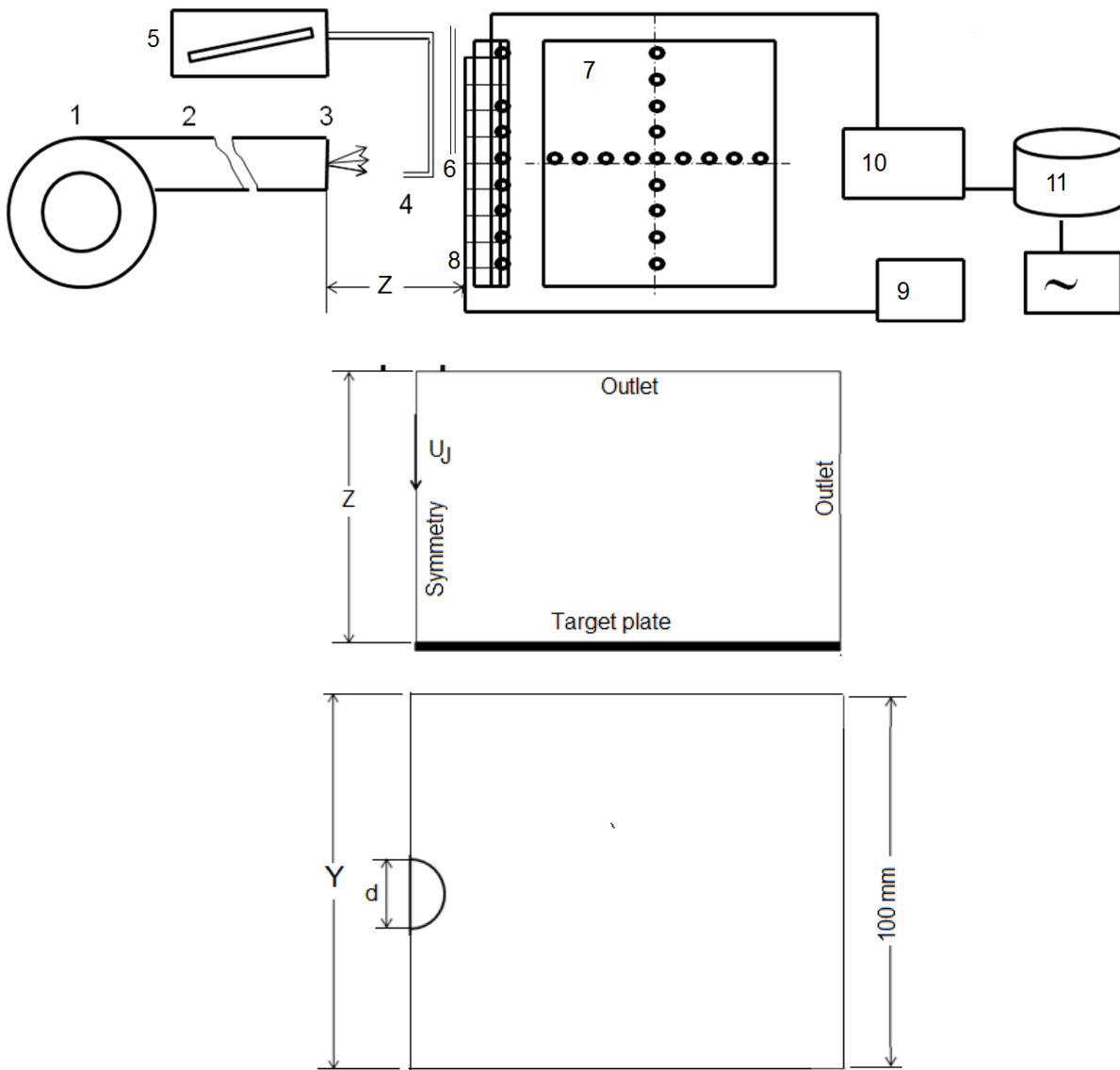


Figure 1 (a)The schematic diagram of experimental facility. (1) centrifugal blower, (2) PVC pipe, (3) orifice plate, (4) Pitot tube for axial velocity measurement, (5) manometer, (6) Pitot tube for radial velocity measurement, (7) heat transfer target plate, (8) thermocouples, (9) temperature recorder, (10) digital multimeter, (11) DC power supply (b) Front and top views of the computational domain

$$q_{total} = q_{conv} + q_{cond} + q_{rad} \quad (2)$$

$$h = q_{conv} / A_s (T_s - T_\infty) \quad (4)$$

and

$$q_{rad} = \varepsilon A_s (T_s^4 - T_\infty^4) \quad (3)$$

The heat loss by conduction is estimated by measuring the temperature at the outer surface of the insulating layer by a number of thermocouples embedded at the outer face of the insulation layer. The calculations show that the heat lost by conduction and radiation is about 10 % of the total input energy respectively. After estimating q_{rad} and q_{cond} , the heat transferred by convection can be calculated from Eq. (2) which can be used to calculate the local heat transfer coefficient as

The data are also used to calculate the average heat transfer coefficient for the whole plate by averaging the local values. The heat transfer target plate (6) is replaced by a pressure target plate made of Plexiglas plate 400 x 400 x 4 mm in size to measure the static pressure distribution using 12 holes of 1.5 mm drilled in radial direction with a distance of 6 mm from each other. All holes are fitted with tubes of 1.5 mm diameter and 30 mm in length t and connected manometer to measure the static pressure distribution on the target plate. Pressure coefficients are calculated for jet impingement velocity of 20 m / sec. The orifice to plate axial distance is adjusted by moving the target plate to give $Z/d = 1 - 8$.

3. CFD Model and Simulation

3.1 Description of Computational Domain and Boundary Conditions

The computational domain shown in Figure 1b includes the orifice and the target plate to model the experimental geometry. The diameters of the orifices considered in this simulation are 5, 10, 20, 30 and 40 mm while $Z/d = 0.5$ to 15. The target plate is maintained at a constant heat flux which is taken from experimental conditions. Half of the actual experimental domain is considered for the simulation due to the geometry and thermal symmetries. A constant pressure-outlet condition is used for the outlet surfaces. The fluid properties was calculated at the mean film temperature $[(T_s + T_\infty)/2]$ for each experimental case. The solution was considered to be converged when the normalized residuals were less than 10^{-5} for continuity, velocity components, energy and turbulence quantities.

3.2 Mathematical Formulation

To simulate flow and heat transfer of the impinging jets, the equations for conservation of mass, momentum with an appropriate turbulence model and thermal energy should to be solved. In this study, the flow is considered as three dimensional, steady, turbulent, incompressible, and axisymmetric with constant properties. The flow is modeled with time-averaged continuity, momentum, and energy equations [12]:

Continuity equation:

$$\frac{\partial(\rho u_i)}{\partial x_i} = 0 \quad (5)$$

Momentum equation:

$$\frac{\partial(\rho u_i u_j)}{\partial x_j} = -\frac{\partial p}{\partial x_i} + \frac{\partial}{\partial x_j} \left[\mu \left(\frac{\partial u_i}{\partial x_j} + \frac{\partial u_j}{\partial x_i} \right) \right] + \frac{\partial(-\rho \overline{u'_i u'_j})}{\partial x_j} \quad (6)$$

Energy equation:

$$\frac{\partial(u_i \rho E)}{\partial x_j} = \frac{\partial}{\partial x_j} \left[\left(k + \frac{c_p \mu_t}{Pr_t} \right) \frac{\partial T}{\partial x_j} \right] \quad (7)$$

Reynolds stresses in the Eq. 6 is modelled using Boussinesq approximation [13]:

$$\frac{\partial(-\rho \overline{u'_i u'_j})}{\partial x_j} = \mu_t \left(\frac{\partial u_i}{\partial x_j} + \frac{\partial u_j}{\partial x_i} \right) - \frac{2}{3} \rho k \delta_{ij} \quad (8)$$

Turbulent viscosity:

$$\mu_t = \frac{\rho C_\mu k^2}{\varepsilon} \quad (9)$$

In present study, the Renormalization-Group (RNG K-ε) turbulence model is employed used as it was used by [9, 11, and 13]. They found that this model reflect the basic features of the impinging jet flow in stagnation point and wall jet regions adequately. The conservation equations for the turbulent kinetic energy k and the dissipation rate ε are:

Turbulence kinetic energy, k :

$$\rho \frac{\partial}{\partial x_i} (k u_i) = \frac{\partial}{\partial x_j} (\alpha_k \mu_{eff} \frac{\partial k}{\partial x_j}) + G_k - \rho \varepsilon \quad (10)$$

Dissipation rate of turbulent kinetic energy, ε :

$$\rho \frac{\partial}{\partial x_i} (\varepsilon u_i) = \frac{\partial}{\partial x_j} (\alpha_\varepsilon \mu_{eff} \frac{\partial \varepsilon}{\partial x_j}) + C_{1\varepsilon} \frac{\varepsilon}{k} G_k - C_{2\varepsilon} \rho \frac{\varepsilon^2}{k} - R_\varepsilon \quad (11)$$

Where

$$G_k = \mu_t S^2, \quad S = \sqrt{2 S_{ij} S_{ij}}, \quad S_{ij} = \frac{1}{2} \left(\frac{\partial u_j}{\partial x_i} + \frac{\partial u_i}{\partial x_j} \right),$$

$$R_\varepsilon = \frac{C_\mu \rho \eta^3 (1 - \eta / \eta_o) \varepsilon^2}{1 + \beta + \eta^3} \frac{\varepsilon^2}{k}, \quad \eta = \frac{S_k}{\varepsilon}$$

The model constants are given by [11]: $C_\mu = 0.09$, $C_{\varepsilon 1} = 1.42$, $C_{\varepsilon 2} = 1.68$, $\alpha_k = \alpha_\varepsilon = 1.393$, $\eta_o = 4.38$ and $\beta = 0.012$.

In addition to the general model formulation, the near-wall treatment can have a significant impact on the accuracy of the results where the hydrodynamics and thermal boundary layers are evolved. It can be divided into two regions; viscous sublayer close to the wall and a fully developed turbulent region at some distance from the wall. The interface between the two regions can be characterized by the value of dimensionless wall distance $y^+ (y U_\tau / \nu) \approx 11.26$ as explained in [14]. The scalable wall function available in

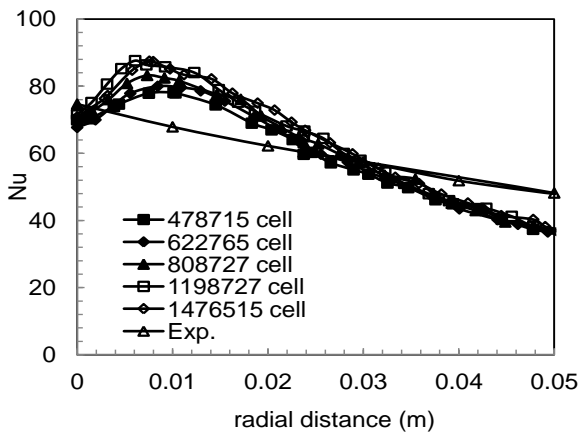
Fluent assumes that the start of turbulent region coincides with edge of viscous sublayer ($y^+ = 11.26$). This option is used in this study to avoid the difficulty of achieving $y^+ > 30$ at the stagnation point and wall jet regions. The idea behind the wall function approach is to apply boundary conditions, based on log-law relations at some distance away from the wall so that the turbulence model equations are not solved close to the wall as discussed in [16]. The simplifications and economies provided by wall functions are especially attractive, and they are widely used in the application of commercial CFD codes to compute the complex turbulent flow problems [12].

4. Results and Discussion

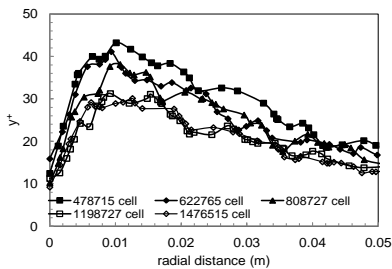
4.1. Grid Independence and Turbulence Models Study

The ANSYS Workbench Meshing tool is used to generate a tetrahedral mesh throughout the computational domain. The grid independence investigation was carried out to obtain with optimum grid size using the RNG k-ε turbulence model. The Nusselt numbers were calculated for 5 different grid sizes to check the effect of the grid size on heat transfer from the target plate for flow from an orifice of $d = 10$ mm at $Z = 60$ mm (Z/d

= 6). The jet velocity, $U_j = 30$ m/s ($Re = 19500$) is used for heat transfer calculation. Figure 2a shows the radial distributions of predicted results of Nu for different grid sizes. The experimental data of Nu is also included in figure 2a for comparison. The corresponding y^+ radial distributions for $U_j = 30$ m/s is given in Figure 2b. The results in Figure 2a show that Nu increased with increasing the number of cells (finer mesh), in particular at the stagnation region. The average Nusselt number increased from 59.3 to 62.7 (cells number = 478715 and 1476515) which is about 6%. This shows that the change is insignificant over the huge change in the cells number.



(a)



(b)

Figure 2 (a) Radial Nu distribution and (b) Radial y^+ distribution for different number of cells ($d = 10$ mm, $Z/d = 6$, $U_j = 30$ m/s).

In contrast, the y^+ values in Figure 2b decreased and become less than 11.26 at the stagnation for cell numbers > 622765 . However, the results from Fluent predictions indicated that the optimum value of the number of cells that produce Nu values close to experimental measurements is 622765 (i.e. cell volume = 0.001855 m³). This is the cell volume which is used to generate the mesh of the computational domains for the different heights (Z).

In addition to the RNG K- ϵ turbulence model which is used in the current study, one simulation for the selected number of cells (622765) has been carried out using the k- ϵ and RSM models to investigate any potential effect of model choice on the prediction of Nusselt number justify this selection. Figures 3a present the Nu from Fluent predictions for flow from an orifice of $d = 10$ mm and $Z = 60$ mm ($Z/d = 6$).

The results show that, Nu values from k- ϵ model are higher by 48.5 %, Nu values from RMS model are higher by 21% but Nu from RNG k- ϵ model are lower by 9.6% than the experimental values at the stagnation point. The discrepancy decreased with r/d which becomes almost zero at $r/d = 2$ and increased again to becomes less than experimental values. The average Nu calculated from the local predicted values using k- ϵ , RSM, RNG k- ϵ and experimental data are 66.25, 59.26, 61.4 and 60.35 respectively. In spite of the average values of Nu from both RNG k- ϵ and RSM are very close to experimental data; but the radial distribution from RNG k- ϵ model is closer to the distribution of experimental data. Therefore, it can be concluded that RNG k- ϵ model is the appropriate model to be used in this study. The discrepancy between the Nu from different turbulence models can be attributed to the difference in the structure of the turbulent intensity (TI) as shown in Figure 3b. The results in Figure 3b show that k- ϵ model gives the highest values of turbulence intensity compared to RSM and RNG k- ϵ model respectively and the peak value appeared at the stagnation point for k- ϵ model moved away in radial direction for RSM and even further for RNG k- ϵ model. The present conclusion is in consistent with previous published work in literature by [11, 13].

4.2. Velocity and Turbulence Intensity Distribution in Free Jet, Impinging Jet and Wall Jet

Figures 4a & 4b present the results of the evolution of the radial velocity distribution of free jet from experimental measurements and Fluent predictions. The comparison between the measurements and predictions shows good agreement ($< 20\%$) for the core region of the jet ($r < d/2$) but the discrepancy increased in the outer region. The discrepancy may be attributed to inaccuracy of the Pitot tube measurements for small velocities.

For $d = 10$ mm, the jet emerging from the orifice is characterized by a high velocity with a fairly flat profile reflecting the existence of the potential flow close to the outlet of the orifice. As the jet moves further, it developed into a free jet with a lower velocity and broader as the positional flow condition vanishes in the region of the free jet zone ($Z \approx 50$ mm). The free jet zone was explained in detail in [15] as follows: The velocity gradients in the jet create a shearing layer at the edges of the jet which transfers momentum laterally outward, pulling additional fluid along with the jet and raising the jet mass flow. In this process, the jet loses energy and the velocity profile is widening spatially and decreases in magnitude in radial direction. If the shearing layer expands inward and reach the centre of the jet prior to reaching the target plate, a region of core decay will be formed. The core decay is the region where the emerging jet becomes sufficiently far from the impingement surface to behave as a free submerged jet. For $d = 20$ mm, Figure 4b shows the development of radial velocity distributions which are different from the results for orifice of $d = 10$ mm. It can be observed that the potential zone with higher velocity is appearing for larger orifice diameter compared to the smaller orifice size for the same axial distance from the orifice. The results also show a gradual change in radial velocity distribution for $d = 20$ mm compared to steep decrease in radial velocity distribution for $d = 10$ mm. It can be seen that the jet centreline velocity decreased by 40% from the jet exit velocity at $Z/d = 6$ for $d = 10$ mm but it decreased by 6% from jet exit velocity at $Z/d = 6$ for $d = 20$ mm. Thus, the potential core become longer as orifice diameter increased for same jet velocity. Similar behaviour was observed experimentally by [17].

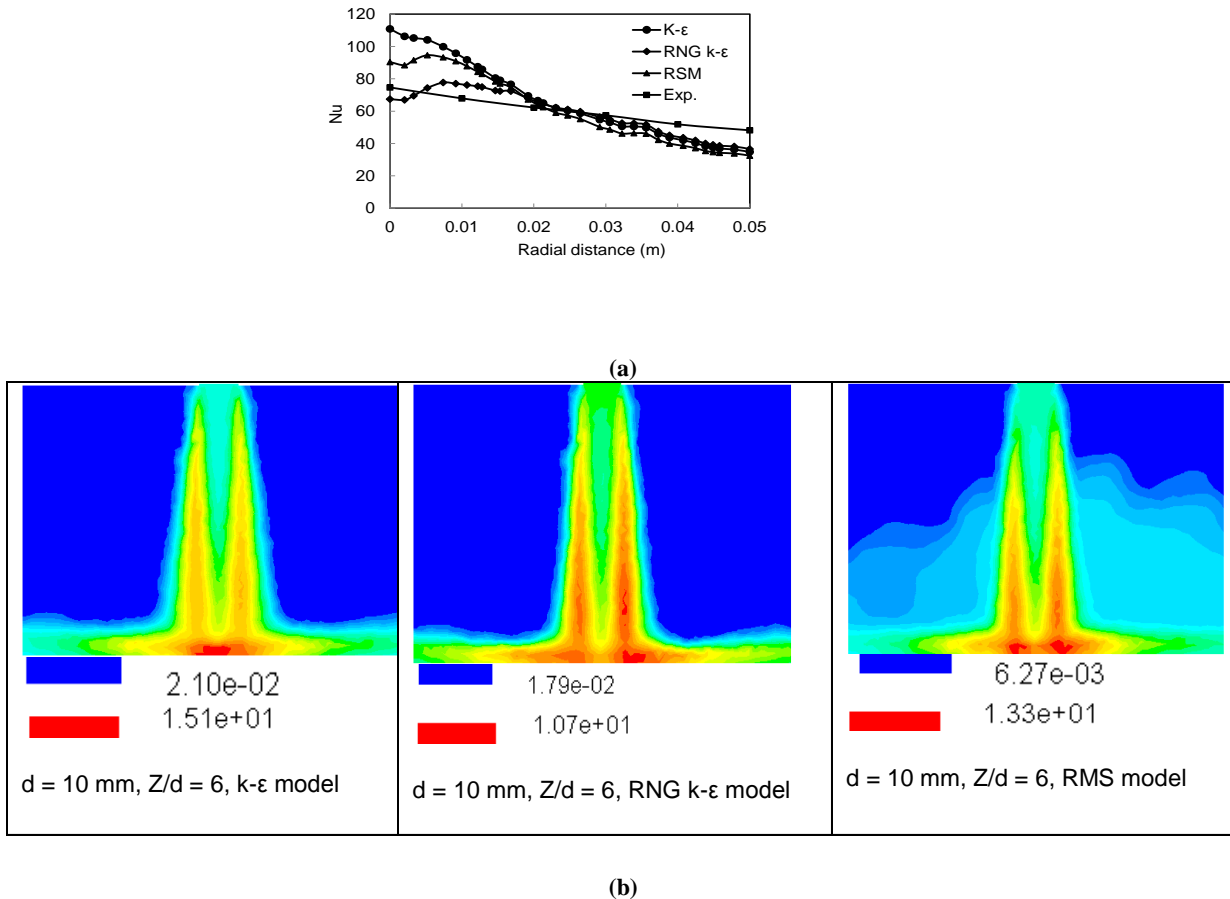


Figure 3 (a) Radial Nu distribution and (b) Turbulence intensity contours for different turbulence models ($d = 10$ mm, $Z/d = 6$, $U_j = 30$ m/s).

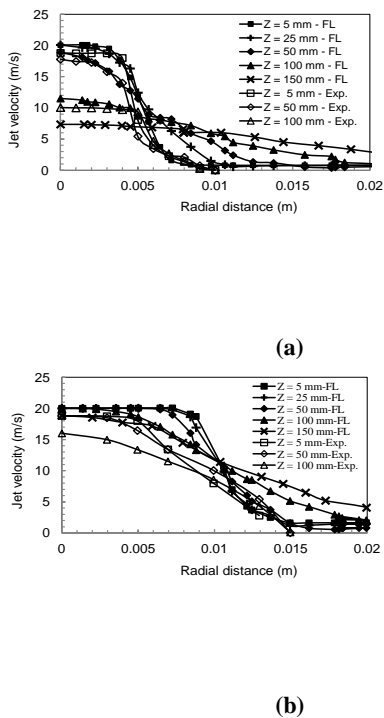


Figure 4 Radial U_j distribution in free jet at $U_j = 20$ m/s and different distances from the orifice $d =$ (a) 10 mm, (b) 20 mm.

As the flow approaches the target plate, the flow is subjected to a strong curvature and very high strain due to the presence of the target plate. The flow experiences an unfavorable static pressure gradient due to rapid deceleration near the wall and after the impingement and it accelerates along the target plate. The axial momentum of the flow impinges on the target plate is converted into radial momentum and the flow resembles a wall jet. The air enters a wall jet region where the flow moves radially outward parallel to the surface of the target plate. The boundary layer within the wall jet begins in the stagnation region, where it has a typical thickness of no more than 1% of the jet diameter as given in [18]. The wall jet has a shearing layer influenced by both the velocity gradient with respect to the stationary fluid at the target plate wall (no-slip condition) and the velocity gradient with respect to the fluid outside the wall jet. Figures 5a, 5b, 5c & 5d present a comparison between the radial wall jet velocities from Fluent predictions and experimental data for different orifice diameters and Z/d ratios.

The results show some discrepancy between Fluent predictions and experimental data but a similar trend can be observed. The discrepancy in the results can be attributed to the turbulence modeling complexity at the stagnation region and near the plate, mathematical models used, mesh construction, boundary conditions set up, and wall treatment function as well as the error in experimental measurements. The reviews of previous studies in [15] support the present finding which showed that a significant difference was observed a number of researchers.

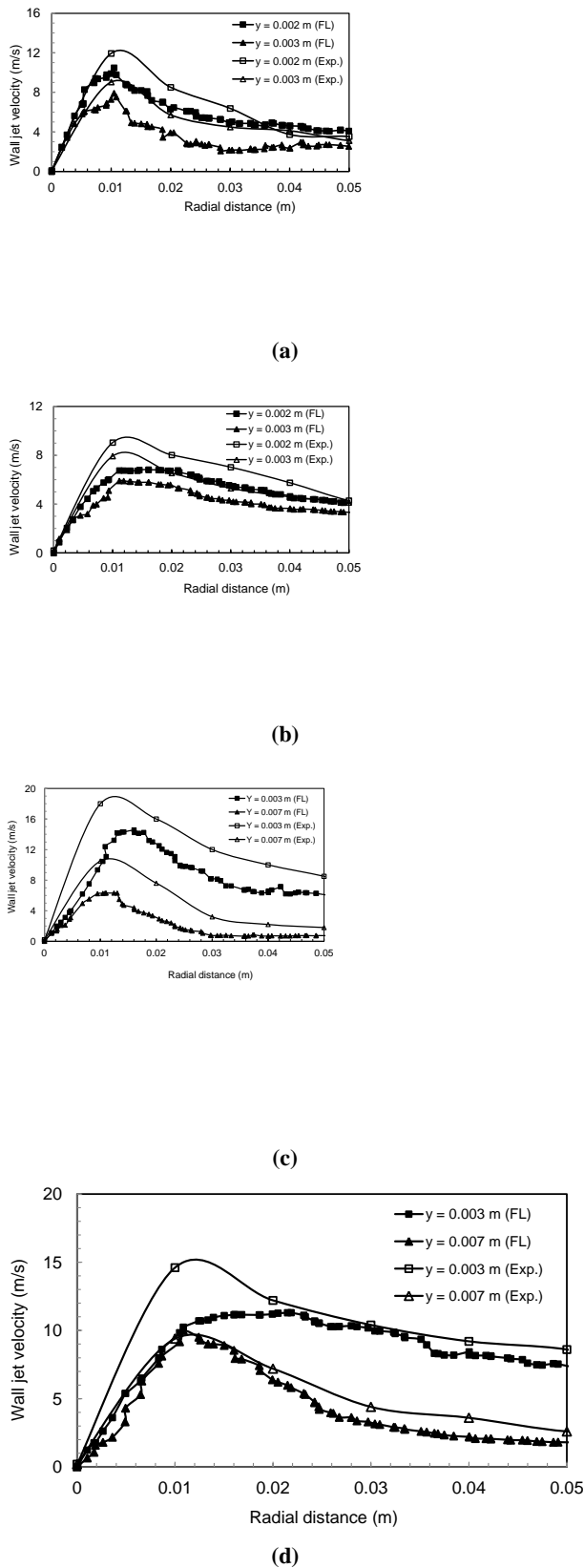


Figure 5 Comparison of radial wall jet velocity distribution from Fluent prediction with experimental measurements at different y values (a) $d = 10$ mm, $Z = 50$ mm, $U_j = 20$ m/s, (b) $d = 10$ mm, $Z = 120$ mm, $U_j = 20$ m/s, (c) $d = 20$ mm, $Z = 50$ mm, $U_j = 20$ m/s, (d) $d = 20$ mm, $Z = 120$ mm, $U_j = 20$ m/s.

The Fluent predictions at stagnation zone clearly show that the wall jet developed within the stagnation zone and reached its maximum velocity at a certain radial distance depend on orifice diameter and Z/d . The results show that the wall jet velocity is higher for orifice diameter of 20 mm compared to 10 mm for $Z = 50$ and 120 mm. The wall jet velocity decreases at larger radial positions as the jet spread away from the centre which can be explained by applying the mass conservation law at different radial positions.

4.3. Pressure Coefficient

The results from Fluent predictions and experimental measurements for orifice diameters of 10 mm at $Z = 5, 50, 70$ and 50 mm from orifice exit for $U_j = 20$ m/s are given in Figure 6a. It can be observed that that pressure coefficient is very close to 1 at the stagnation point for $Z \leq 70$ mm but decreased to small values for $Z > 70$ mm. The Fluent predictions and experimental measurements are in good agreement for $Z \leq 70$ mm but the discrepancy increased for $Z > 70$ mm. Figure 6b present the C_p distribution for $d = 20$ mm at $Z = 5, 50, 70$ and 50 mm from orifice exit for $U_j = 20$ m/s. An interesting behavior of the flow can be observed at small Z value ($Z/d = 0.5$) where $C_p > 1$. The higher value can be attributed to the critical distance between the orifice exit and the target plate required to avoid the effect of stagnation condition on the free jet flow. Similar findings was reported by [8] as $C_p = 2.5$ for $Z/d = 0.2$. The results also indicated that C_p distributions is a function of orifice diameter and analogous to the radial velocity distributions of the jet at same location which are supported by the experimental results from [19].

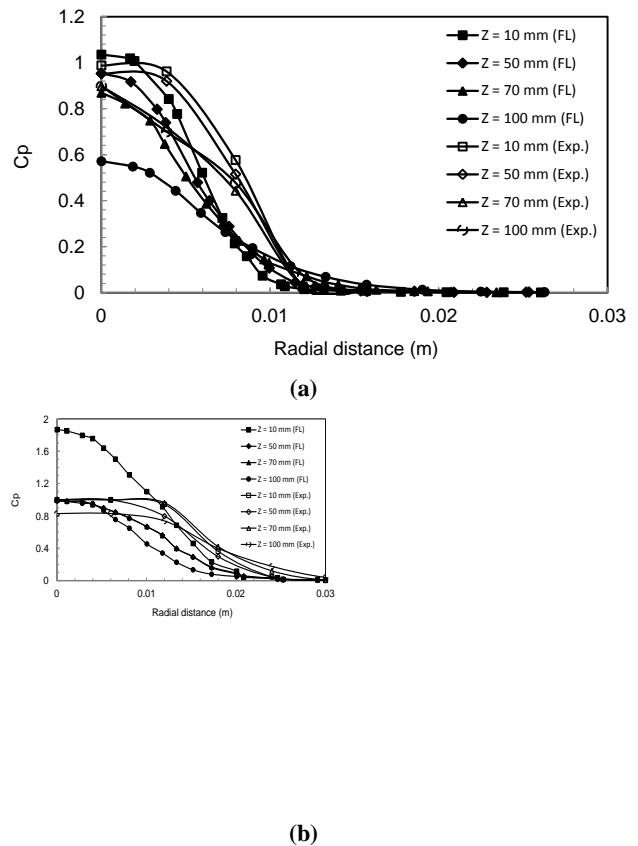


Figure 6. Comparison of pressure coefficient distribution at $U_j = 20$ m/s and different axial distances of (a) $d = 10$ mm, (b) $d = 20$ mm.

4.4. Heat Transfer from the Target Plate

The local heat transfer coefficients and the Nusselt numbers for $d = 5, 10$ and 20 mm at different Z values were calculated experimentally from the heat flux and temperature distributions on the target plate. The Fluent was also used to simulate the experimental cases to predict the Nu values. The simulation was also used to extend work to cover larger orifice diameters ($d = 30$ and 40 mm) and higher Z/d values (Figure 7_ present the results from Fluent predictions and experimental measurements for $d = 10, 5$ and 20 mm at different Z/d ratio ($2 \leq Z/d \leq 15$), respectively. Despite the apparent difference in the shape of the Nu profiles from the Fluent predictions compared to experimental measurements, the discrepancy in average values (Nu_{av}) is less than 20%.

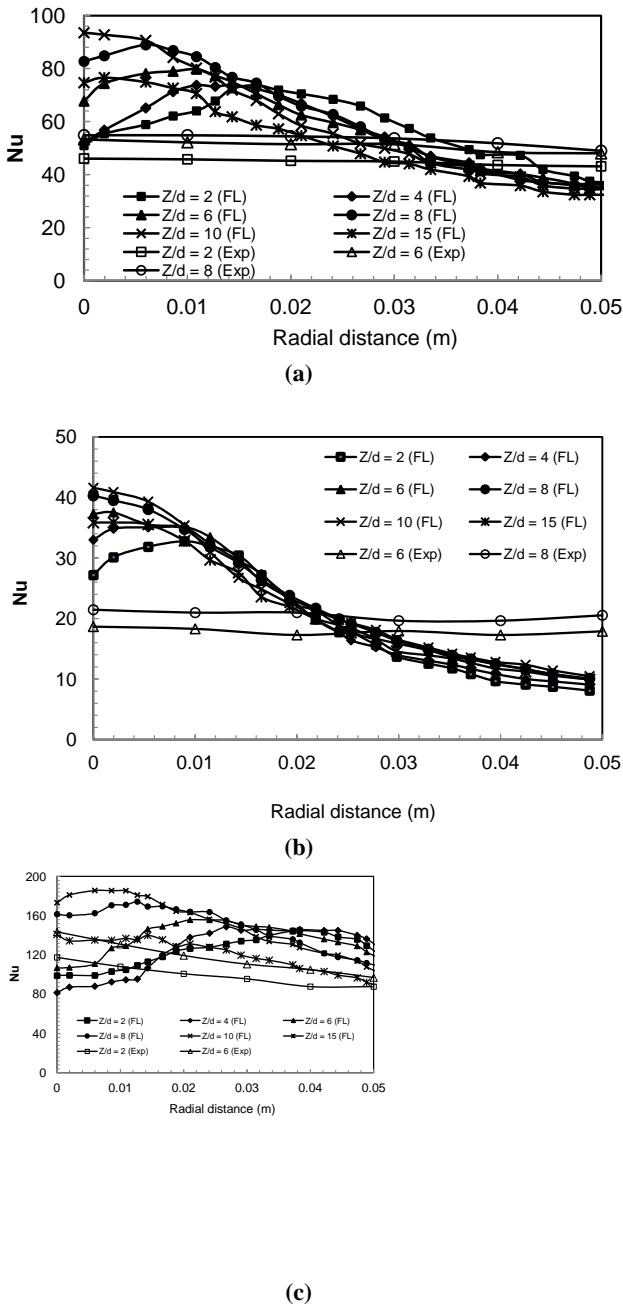


Figure 7. Radial Nu distribution with $U_j = 30$ m/s and Z/d ratio (a) $d = 10$ mm, (b) $d = 5$ mm, (c) $d = 20$ mm.

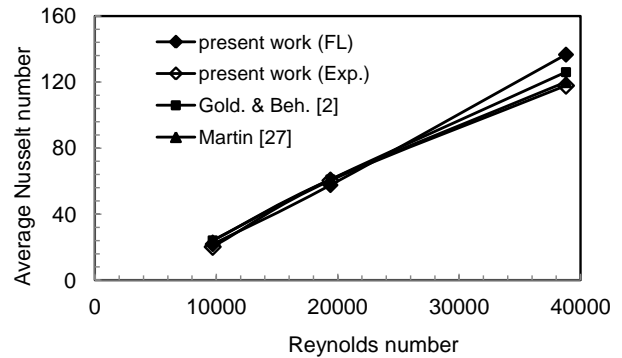


Figure 8. Comparison of Average Nusselt numbers from Fluent predictions and experimental data with literature ($Z/d = 6$)

Figure 8 present a comparison of average Nusselt numbers with Reynolds numbers from the present work and literature [2, 18]. It reveals that the present experimental data and Fluent predictions are in good agreement with the published data in literature.

To discuss the heat transfer at different Z/d ratio, the results from the orifice of $d = 10$ mm is selected. The results in Figure 9 show that Nu distributions have peaks at different radial distances from stagnation point which depend on the flow conditions of each case ($d, Z/d$). The turbulence contours in

Figure 9 for $d = 10$ mm and $Z/d = 2, 6, 10$ and 15 correspond to heat transfer cases in Figure 7a. The maximum (red) and minimum (blue) values are given underneath the contours to show the range for each case from Fluent predictions. In general the maximum value of TI increased with Z/d ratio reaching its highest value at $Z/d = 10$ then decreased for higher Z/d values. The results also show that the location of the maximum turbulence intensity change from $r = 0.016$ at $Z/d = 2$ to $r = 0$ at $Z/d = 10$ then to $r = 0.002$ at $Z/d = 15$. By comparing the results from Figure 7a and Figure 7e, it can be observed that the radial location of the maximum Nusselt number correspond to the location of the maximum turbulence intensity. By calculating the average values of the Nusselt numbers in Figure 7a, it was found that $Z/d = 8$ gives the highest Nu in spite of the higher value of turbulence intensity at higher Z/d values ($Z/d = 10$ and 15). This may be attributed to the optimum flow conditions where the potential core flow in the jet is disappeared and the turbulence intensity reached it maximum values.

To understand the effect of orifice diameter on Nu, Figures 7b and 7c show the Fluent predictions and experimental Nu for $d = 5$ and 20 mm at different Z/d values. The results show that Nu increased with Z/d which is similar to the trend of results for $d = 10$ mm in Figure 7a. By comparing the results from the three orifice diameters, it can be observed that Nu distributions become more uniform with higher d values as the peak is almost disappeared for $d = 20$ mm. This remarkable change may be attributed to the change in radial distribution of TI as demonstrated in the contours given Figure 9 at $Z/d = 6$ (Right column).

Figure 10 present the variation of Nu_{av} with Z/d for $d = 5, 10$ and 20 mm. The results show that the average Nu increases as the orifice diameter increased. The results also show that

Nusselt number slowly increased with Z/d to reach its peak value at $Z/d \approx 8$ then start decreasing. This behavior is a result of combined effect of velocity and turbulence distributions close to the target plate surface where a boundary layer developed with wall jet evolution. The present results are supported by a similar experimental data reported by [17]. To examine the effect of the orifice diameter on the heat transfer for the same Reynolds number, Figure 11 present a predicted Nusselt numbers calculated for $d = 5, 10, 20, 30$ and 40 mm at

$Re = 19500$ at $Z/d = 6$. The results show that the peak in Nu move from stagnation point for $d = 5$ mm outward in radial direction with a distance equal to orifice diameter. The results show that the average Nu values changed significantly when the orifice diameter increased for $d \leq 30$ mm which become very small for $d > 30$ mm ($d/Nu_{av} = 5/31.5, 10/52.3, 20/77.7, 30/86.5$ and $40/90.5$). A similar findings was reported by [1] for small orifices diameters ($d < 5$ mm).

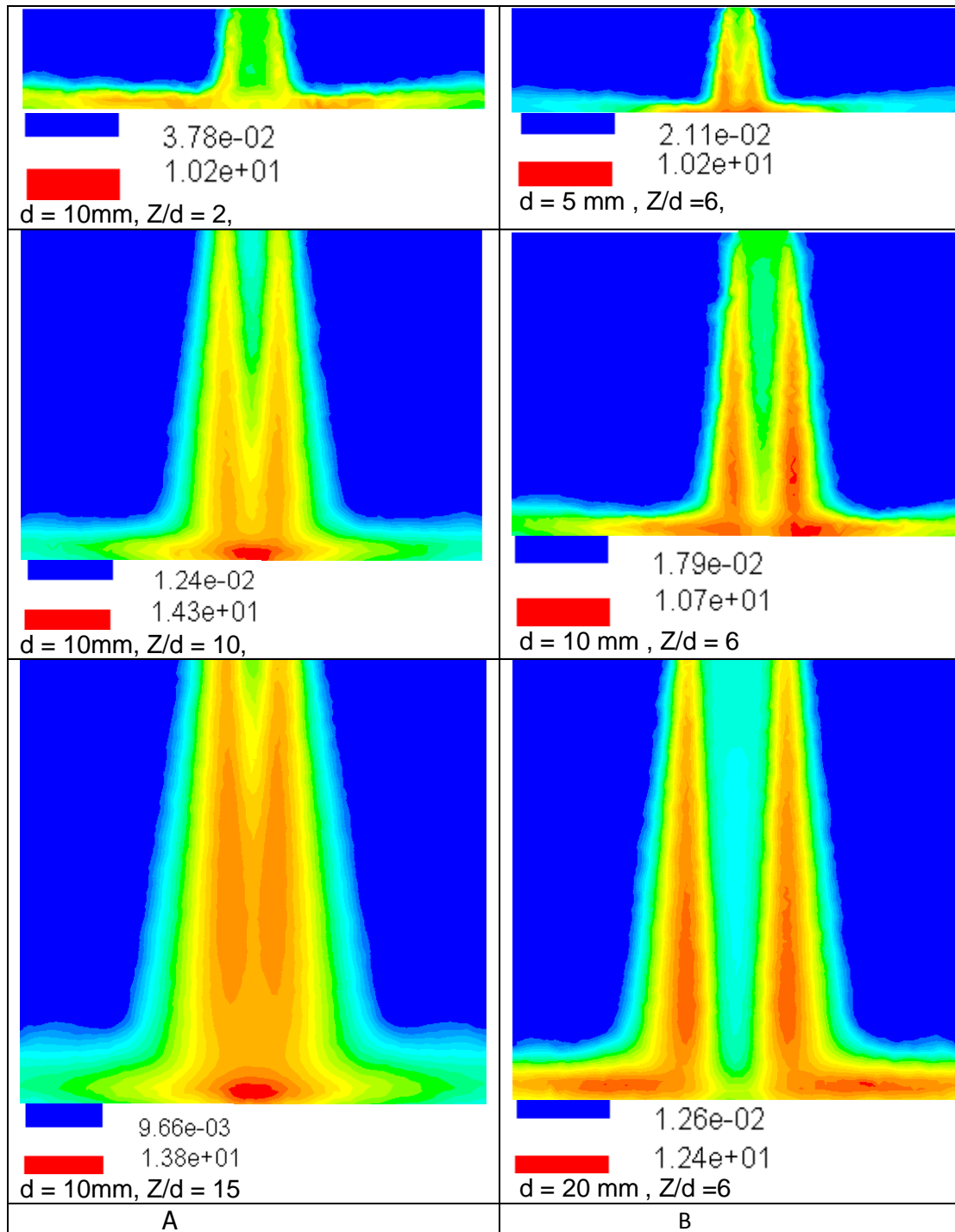


Figure 9. Turbulence intensity contours for $U_j = 30$ m/s. A) $d = 10$ mm and $Z/d = 2, 10, 15$; b) $Z/d = 6$ and $d = 5, 10, 20$ mm.

5. Conclusions

Numerical and experimental investigation of the flow structure and heat transfer of impinging jet on target plate has been performed. The study covers the jet velocity, wall jet velocity, pressure coefficient and Nusselt number for five different orifices ($d = 5, 10, 20, 30$ and 40 mm) and different Z values. The main conclusions from the investigation are:

1. The classical approach used in deterring the mesh number (cell volume) based on successive refinements so that the solution of all variable unchanged is not applicable in this study. The heat transfer coefficient, in particular, continue to increase with finer mesh while y^+ decreases indicate the importance of experimental data to validate the mesh quality (cell volume) required to produce the best possible data from the simulations.
2. The variation of y^+ from the stagnation in radial direction affects the simulation accuracy for the different region on the target plate.
3. The RNG $k-\epsilon$ turbulence model produce better Nusselt number compared to other models when validated against experimental measurements.
4. The radial velocity distributions of the free jet changed from S curve profile to parabolic profile at higher values of d and Z/d
5. The radial turbulence intensity distribution in free jet have saddle shape with peak values at radial distance approximately equal to $0.6d$ to a parabolic shape when for $Z/d \geq 5$.
6. With the existence of pressure gradient in the stagnation zone, the wall jet velocity increased with radial direction to reach a maximum value at radial distance depend on d and Z/d then decreases at larger radial positions based on mass conservation law at different radial positions. The flow can be considered as laminar flow at the stagnation zone.
7. The radial pressure coefficient distributions have a similar shape of velocity distribution which is measured at the same distance Z from the orifice exit. It has a peak value at stagnation point and gradually decreases in the radial direction. The larger orifice diameters give high values of C_p at the same value of Z .
8. Heat transfer rate, i.e. Nu moderately increased with Z/d to reach a maximum at $Z/d = 8$ then start decreasing. The larger orifice diameter gives higher values of heat transfer coefficients compared to smaller orifice diameter at same Z/d values and jet velocity.
9. For the same Re , the Nu increased with orifice diameter due to the modification in velocity and turbulence structure.

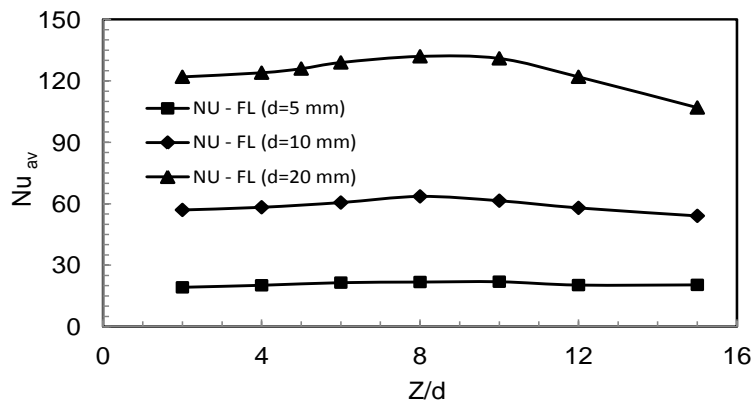


Figure 10. Variation of average Nusselt number (Nu_{av}) with Z/d ratio for $d = 5, 10$ and 20 mm.

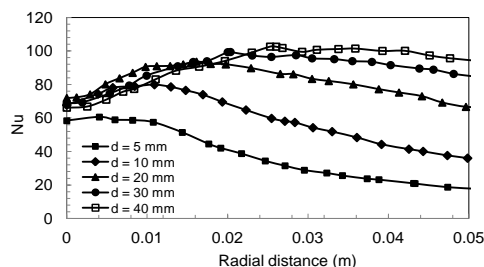


Figure 11. Radial Nu distribution for different orifice diameters and same Reynolds number ($Re = 19500$).

Nomenclature:

| | |
|------------|--|
| A_s | Plate surface area (m ²) |
| C_p | Pressure coefficient ($\Delta P/0.5\rho U_j^2$) |
| c_p | Specific heat capacity at constant pressure (J/kg K) |
| D | Orifice Diameter (mm) |
| E | Total energy (J) |
| h | Heat transfer coefficient (W/m ² K) |
| I | DC electrical Current (A) |
| K | Thermal conductivity (W/m K) |
| k | Turbulence kinetic energy (m ² /s ²) |
| Nu | Nusselt number (hd/K_a) |
| ΔP | The difference between the local pressure on target plate and the atmospheric Pressure (N/m ²) |
| Pr_t | turbulent Prandtl number |
| q_{cod} | Heat transfer by conduction (W) |
| q_{conv} | Heat transfer by convection (W) |
| q_{rad} | Heat transfer by radiation (W) |
| R | Radial Distance from the stagnation point (mm) |
| Re | Reynolds number ($U_j d/\mu$) |
| T | Temperature (K) |
| T_s | The local surface temperature on the target plate (°C) |
| T_∞ | The ambient temperature of the impinging jet (°C). |
| U_j | Jet Velocity (m/s) |
| U_τ | Friction velocity (m/s) |
| V | Voltage (V) |
| Y | Orifice-to-plate distance (mm) |
| y | Distance from the wall (m) |
| y^+ | Dimensionless distance from the wall |
| ϵ | Dissipation rate of turbulence kinetic energy (m ² /s ³) |
| μ | Dynamic viscosity (N s/m ²) |
| μ_t | turbulent viscosity (kg/m s) |
| ν | Kinematic viscosity (m ² /s) |
| ρ | Density (kg/m ³) |

References

[1] San, J. Y., Huang, C. H., And Shu, M. H., 1997, "Impingement Cooling of a Confined Circular Air Jet," *Int. J. Heat Mass Transfer*, **40** (6), pp. 1355-1364.

[2] Goldstein, R. J., and Behbahani, A. I., 1982, "Impingement of Circular Jet with and without Cross Flow," *Int. J. Heat Mass Transfer*, **25** (9), pp.1377-1382.

[3] Lee, D., Greif, R., Lee, S. J., and Lee, J. H., 1995, "Heat Transfer from a Flat Plate to a Fully Developed Asymmetric Impinging Jet," *Transactions of the ASME*, **117**, pp. 772-776.

[4] Lytle, D., and Webb, B.W., 1994, "Air Jet Impingement Heat Transfer at Low Nozzle Plate Spacing," *Int. J. Heat Mass Transfer*, **37** (12), 1687-1697.

[5] Anwarullah, M., Vasudeva Rao, V., Sharma K.V, 2012, "Effect of Nozzle Spacing on Heat Transfer and Fluid Flow Characteristics of an Impinging Circular Jet in Cooling of Electronic Components", *Int. J. of Thermal & Environmental Engineering*, **4** (1), pp. 7-12

[6] Behina, M., S., Parneix, Y., Shabany, Y., and Durbin, P. A., 1999, "Numerical Study of Turbulent Heat Transfer in a Confined and Unconfined Impinging Jets," *Int. J of heat & fluid flow*, **20**, 1-9.

[7] Behina, M., S., Parneix, Y., and Durbin, P. A., 1998, "Prediction of Heat Transfer in an Axisymmetric Turbulent Jet Impinging on Flat Plate," *Int. J of heat and mass transfer*, **41**(12). pp 1845-1855.

[8] Baydar, E., and Ozmen, Y., 2005, "An Experimental and Numerical Investigation on a Confined Impinging Air Jet at High Reynolds Numbers," *Applied thermal engineering*, **25**, pp. 409-421.

[9] Ramezanpour, A., Mirzaee, I., Firth, D., Shirvani, H., 2007, "A Numerical Heat Transfer Study of Slot Jet Impinging on an Inclined Plate," *Int. J. Numer. Methods Heat Fluid Flow*, **17**, 661-676.

[10] Angioletti, M., Nino, E., and Ruocco, G., 2005, "CFD Turbulent Modeling of Jet Impingement and its Validation by Particle Image Velocimetry and Mass Transfer Measurements." *International Journal of Thermal Sciences*, **44**, pp. 349-356.

[11] Pulat, E., Kemal, M., Etemoglu, I. A. B., and Can, m., 2011, "Effect of Turbulence Models and Near-Wall Modeling Approaches on Numerical Results in Impingement Heat Transfer, Numerical Heat Transfer," Part B, **60**: pp. 486-519.

[12] ANSYS Fluent, <http://www.ansys.com/Industries/Acaemic/Tools/Citations>.

[13] Heck, U., Fritsching, K., and Bauckhage K., 2001, "Fluid Flow and Heat Transfer in Gas Jet Quenching of a Cylinder," *Int. J. Numer. Methods Heat Fluid Flow*, **11**, pp. 36-49.

[14] Jayatilleke, C. L. V., 1969, "The Influence of Prandtl Number and Surface Roughness on the Resistance of the Laminar Sublayer to Momentum and Heat Transfer," *progress in heat transfer*, **1**, pp. 193-329.

[15] Zuckerman, N., and Lio, N, 2006, "Jet Impingement Heat Transfer: Physics, Correlations and Numerical Modelling," *Advances in Heat Transfer*, **39**, 565-631

[16] Launder, B. E., and Spalding D. B., 1972, "Lectures in Mathematical Models of Turbulence," Academic Press, London.

[17] Fleischer, A. S., and Nejad, S. R., 2004, "Jet Impingement Cooling of a Discretely Heated Portion of a Protruding Pedestal with a Single Round Air Jet," *Experimental thermal and fluid science*, **28**, pp 893-901.

[18] Martin, H., 1977, "Heat and Mass Transfer between Impinging Gas Jets and Solid Surfaces," *Advances in heat transfer*, **13**, pp. 1-60.

[19] Guo, Y., and Wood, D. H., 1996, "Measurement in the Vicinity of Stagnation Point," *Experimental thermal and fluid science*, **13**, 364-373.